Thin Solid Films 717 (2021) 138440

Contents lists available at ScienceDirect

Thin Solid Films

journal homepage: www.elsevier.com/locate/tsf

Fabrication and characterization of copper (II) oxide/iron (III) oxide thin film heterostructures for trace arsenic (III) removal in water

Elizabeth C. Pastrana [a,*], Steveen J. Loarte [a], Carlos D. Gonzales-Lorenzo [b], Roxana Y.P. Alta [c], Hugo A. Alarcón [a]

[a] Center for the Development of Advanced Materials and Nanotechnology, Universidad Nacional de Ingeniería, P.O. Box 31-139, Av. Túpac Amaru 210, Lima, Perú
[b] Institute of Physics, University of São Paulo, Rua do Matão, Travessa R, 187, CEP 05508-090 São Paulo, SP, Brazil
[c] Biomet Research Group, Facultad de Ciencias, Universidad Nacional de Ingeniería, P.O. Box 31-139, Av. Túpac Amaru 210, Lima, Perú

ARTICLE INFO

Keywords:
Arsenic adsorption
Copper oxide
Heterostructure
Iron oxide
Thin film

ABSTRACT

In this study, nano-heterostructures based on copper (II) oxide/iron (III) oxide (CuO/α-Fe_2O_3) thin films were fabricated by a dip-coating technique using aqueous solutions. The heterostructures were deposited on fluorine-doped tin oxide glass substrates varying the CuO film thickness. From a detailed characterization using Fourier transform-infrared and X-ray diffraction the formation of CuO (tenorite)/α-Fe_2O_3 (hematite) was demonstrated. Atomic force microscopy provided valuable information on the growth of α-Fe_2O_3 crystals in the heterostructure with a conical-shaped surface. Meanwhile, the field emission scanning electron microscopy cross-section images confirm the formation of well-defined CuO layers under the α-Fe_2O_3 layers. The optical band gap energies for the heterostructures obtained were estimated from the diffuse reflectance spectra and ranged from 1.41 to 1.51 eV. Photoluminescence analysis revealed an improved separation and faster transfer of photogenerated electrons and holes for the heterostructures. The removal arsenic from an aqueous solution was achieved through the direct adsorption for As(III) and visible light oxidation to As(V). An enhancement of removal efficiency of As(III) for the heterostructures fabricated compared to pristine oxides was obtained.

1. Introduction

Arsenic contamination in natural water has become one of the most serious health problems in recent years [1,2], due to its high toxicity and carcinogenicity [2]. Arsenic is present in four different oxidation states: (-III), (0), (III), and (V) [3], being arsenate (AsO_4^{3-}) and arsenite (AsO_3^{3-}) the two inorganic forms present in natural waters [4]. Species formed by As(V) are presented just as AsO_4^{3-}, $HAsO_4^{2-}$, H_2AsO^{4-} under oxidizing conditions (aerobic environments) [5], meanwhile As(III) appear as As $(OH)_3$, $As(OH)_4^-$, AsO_2OH^{2-} and AsO_3^{3-} species under reducing conditions (anaerobic environments) [6]. Furthermore, As(III) species are more soluble, toxic, and difficult to immobilize compared to the oxidized form As(V) [7], thus they demand more attention.

To date, various technologies have been developed to remove arsenic [8–10]. Among these techniques, adsorption is one of the most approaches used for these purposes [11,12]. Ferric oxides are highly preferred for arsenic removal (especially for arsenate), owing to its high affinity to arsenic, ease of synthesis, low cost, and nontoxicity [13–15]. In particular, Hematite (α-Fe_2O_3), which is an n-type semiconductor with a narrow bandgap of 1.9–2.2 eV, has a greater potential for contaminant adsorption due to its stability [16]. However, the low affinity and photocatalytic activity of iron oxide-containing adsorbents toward As(III) make necessary the effective elimination of arsenic in water under irradiation of visible light [15]. Therefore, it is a challenge to develop efficient, reliable and economical adsorbent for As(III) removal through photooxidation and adsorption.

Copper oxide is a p-type semiconductor with a narrow bandgap of 1.3 to 2.21 eV [17], previous studies investigated their high photoactivity with a theoretical photocurrent density of 35 mA/cm^2 [18]. Their photoconductive and photochemical properties have made CuO a good candidate for the fabrication of heterostructures [19,20]. Moreover, CuO is an effective arsenic adsorbent because it works at a large pH and not have interferences in the presence of competing anions [21].

Recent works reported an enhancement in photoelectrochemical and photocatalytic performance of hematite nanostructures by Cu-doping [22,23]. In addition, α-Fe_2O_3 is also used together with CuO

* Corresponding author.
E-mail address: epastrana@uni.edu.pe (E.C. Pastrana).

https://doi.org/10.1016/j.tsf.2020.138440
Received 21 July 2020; Received in revised form 18 October 2020; Accepted 14 November 2020
Available online 20 November 2020

semiconductor [24–26] due to their physical, chemical, and photochemical properties, which produce an effective separation and transfer of the photogenerated charge carriers under irradiation of light, inhibiting the recombination process [26]. Besides, nano-scaled adsorbents have a higher adsorption capacity for arsenic than larger particles [27].

Based on the above considerations, the present paper mainly focused on the arsenic (III) removal by CuO/α-Fe_2O_3 nano-heterostructures, which were fabricated through dip-coating and rarely reported. The hematite layers were placed at the top of the surface of the composites to improve arsenic removal. The nanostructured adsorbents formed by this process were optimized by varying the CuO thickness.

2. Experimental

2.1. Materials

Iron nitrate ($Fe(NO_3)_3.9H_2O$), ethylene glycol ($HOCH_2CH_2OH$), diethanolamine 99 % ($HN(CH_2CH_2OH)_2$) and sodium arsenite ($NaAsO_2$) were purchased from Sigma-Aldrich, USA. Meanwhile, copper acetate 99 % ($Cu(CO_2CH_3)_2$) and isopropyl alcohol ($(CH_3)_2CHOH$) were purchased from Merck, USA. All chemicals were used without further purification and were of analytical grade. Ultrapure water was used in the whole experimental process. Fluorine-doped tin oxide (FTO) glass conductive plates of 3.5 cm × 2.5 cm of area and 7 Ω/cm^2 of resistance were used as substrates for the deposition of the heterostructures.

2.2. Fabrication of CuO/α-Fe_2O_3 heterostructures

CuO and Fe_2O_3 precursor solutions were prepared by the following procedure. The CuO precursor solution was prepared according to Shariffudin et al. [28] by dissolving copper acetate in isopropyl alcohol and then adding diethanolamine dropwise into the solution, while the α-Fe_2O_3 precursor solution was prepared based on the method reported by Karakuscu and Ozenbas [29] by dissolving iron nitrate in ethylene glycol at 80 °C for 1 h under stirring.

The CuO/α-Fe_2O_3 thin films were prepared by the following procedure shown in Fig.Fig. 1. CuO films with a different number of layers were deposited on FTO glass conductive plates by dip-coating using CuO precursor solution and then were calcinated at 500 °C for 1 h with a heating rate of 10 °Cmin^{-1}. Afterward, an α-Fe_2O_3 film was deposited on top of the deposited CuO film using Fe_2O_3 solution, where dip-coating and heat treatment at 600 °C for 1 h with a heating rate of 10 °Cmin^{-1} were carried out. Finally, the heterostructure obtained was annealed at 600 °C for 3 h for the aim of recrystallization. The CuO number of layers fabricated was varied in 12, 24 and 36 to obtain different thicknesses of the thin films. Whereas, the deposition process of α-Fe_2O_3 was repeated twenty times for all heterostructures. The heterostructures fabricated with 12, 24 and 36 layers of CuO were labeled as Het 12, Het 24 and Het 36, respectively.

2.3. Characterizations of the deposited samples

The obtained nano-heterostructures were characterized using a Shimadzu IR Prestige-21 Fourier transform infrared (FT-IR) spectrophotometer over a range of 400 to 700 cm^{-1}. The crystal structures were measured by X-ray diffraction (XRD) on a Bruker D8 Advance diffractometer. The 2θ range was from 20 to 70 degrees with CuKα radiation (λ = 1.5418 Å). The surface topography and roughness were observed by Bruker Dimension Icon atomic force microscope (AFM), operating in PeakForce Tapping mode with a ScanAsyst Air (Bruker) tip. The morphology of the prepared samples was visualized by Hitachi SU-8230 field emission scanning electron microscope (FE-SEM) with operation voltage of 3 kV. The constituent elements present in the films were determined by XFLASH 6160 Energy dispersive X-ray spectrometer (EDS) carried out with operating voltage of 6 kV. The optical band gap energies of the samples were estimated from the diffuse reflectance spectra (DRS) measured using a Shimadzu UV-2600 UV-vis spectrophotometer recorded in the range of 200–800 nm. The photoluminescence measurements (PL) were recorded at room temperature using Horiba Fluoromax-4 spectrofluorometer equipped with a 150 W xenon lamp and excited with a 350 nm laser source.

2.4. Batch adsorption experiment

The trace arsenic removal abilities on CuO/α-Fe_2O_3 nano-heterostructures were measured through adsorption experiments performed on capped transparent borosilicate vials, where the films were placed and covered with 100 mL of an arsenic solution. The initial concentration of arsenic was 1 mgL^{-1}. The pH value of the solution was adjusted to pH = 3.1 and controlled in all assay using a pH meter with an Ag/AgCl electrode with 0.1 M HCl solution. The tests were accomplished under magnetic stirring at 600 rpm to provide homogenization and transport towards the surfaces of the film. The temperature was controlled at 20 °C using a cooling reflux system. In dark tests, the arsenic solution was kept in the total absence of light. In contrast, on light tests, the arsenic solution with the sample immersed was kept

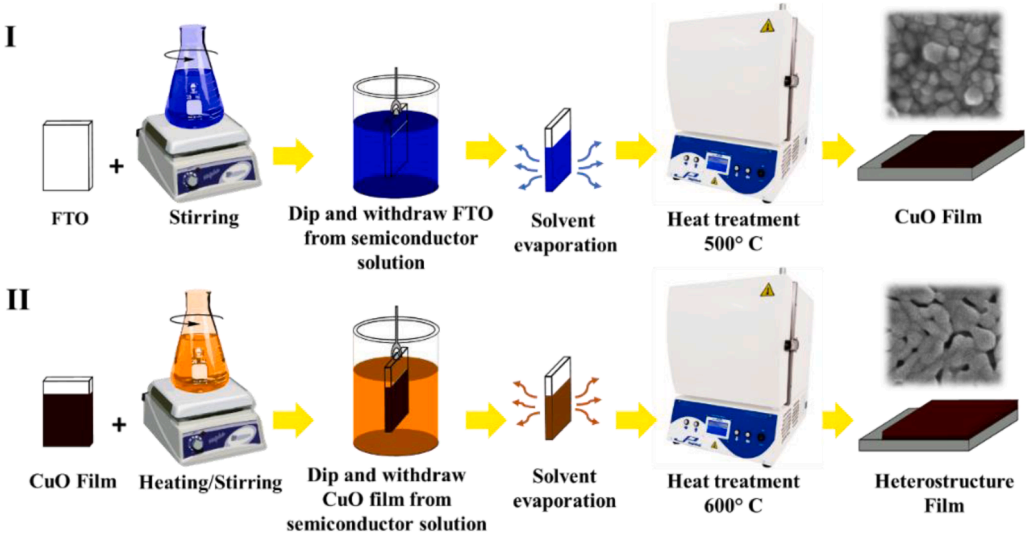

Fig. 1. Schematic diagram for the process to produce the CuO/α-Fe_2O_3 thin film by dip-coating: (I) Deposition of copper oxide on FTO glass and (II) deposition of α-Fe_2O_3 on a CuO thin film.

under stirring in dark and immediately was irradiated with 220 W OSRAM Ultravitalux lamp where 80 Wm^{-2} of intensity was measured with a radiometer. During the irradiation, 1 mL of the treated solution was collected each 20 min in order to analyze the arsenic concentration. The speciation of As(III) and As(V) was determined by the High performance liquid chromatography (with Hamilton PRP X100 anionic exchange column)-HG-atom fluorescence technique using the Millennium PSA Arsenic Analyzer (PSA Analytical). The arsenic removal activity of α-Fe_2O_3 thin film and the heterostructures fabricated with different CuO thicknesses were compared.

3. Results and discussion

3.1. Fourier transformed infrared spectroscopy

FT-IR analysis, shown in Fig. 2, was carried out to confirm the phase composition of the CuO/α-Fe_2O_3 heterostructures in the range at 400–800 cm^{-1}. It should be noted that the bands around at 417 cm^{-1} and 470 cm^{-1} in the CuO and heterostructures spectra are ascribed to the formation of metal-oxygen stretching of CuO nanostructure [30], which are in good agreement with previous results [30–32]. Moreover, the band located approximately at 517 cm^{-1} in the Fe_2O_3 spectrum are associated to Fe-O vibration [33], this band appears blue-shifted 10 cm^{-1} in the heterostructures spectrums, due mainly to morphological changes (size and shape) of the nanoparticles forming the CuO/α-Fe_2O_3 heterostructures because of the interaction between both pure oxides [34]. The band around at 660 cm^{-1} also associated with the Fe–O vibration [35] was obtained in the heterostructures spectra.

3.2. X-ray diffraction analysis

The crystal structure and phase purity of the samples obtained were characterized by XRD analysis. The XRD patterns of the α-Fe_2O_3 films, CuO films and CuO/α-Fe_2O_3 nano-heterostructures are shown in Fig. 3. The figure reveals two main diffraction peaks at 35.8° and 38.6° corresponding to the (110) and (111) crystallographic planes of α-Fe_2O_3 and CuO, respectively. The XRD patterns can be readily indexed to the hematite (JCPDS card No. 33-664) [36] and tenorite (JCPDS card No. 45-0937) [37] crystal phases. Other diffraction peaks of impurity phases were not detected, indicating the pure phase formation of pristine oxides. Moreover, the diffractograms of the CuO/α-Fe_2O_3 heterostructures does not show other diffraction peaks than those of CuO and α-Fe_2O_3 films, implying the co-existence of both oxides in the heterostructures.

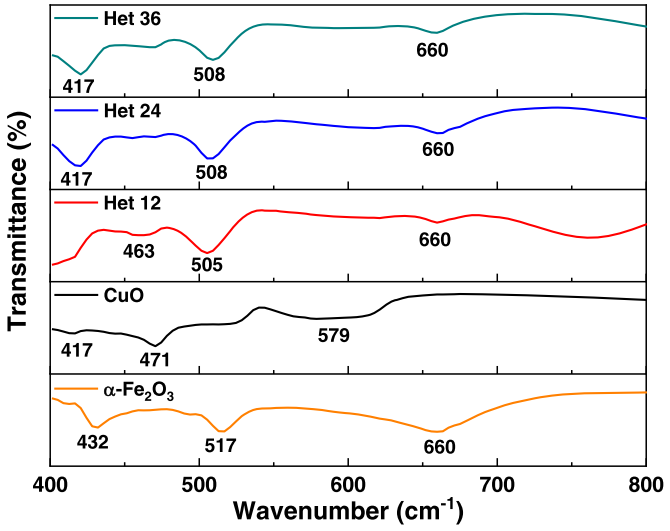

Fig. 2. FT-IR spectra of CuO/α-Fe_2O_3 heterostructures (Het 12, Het 24 and Het 36), CuO and α-Fe_2O_3.

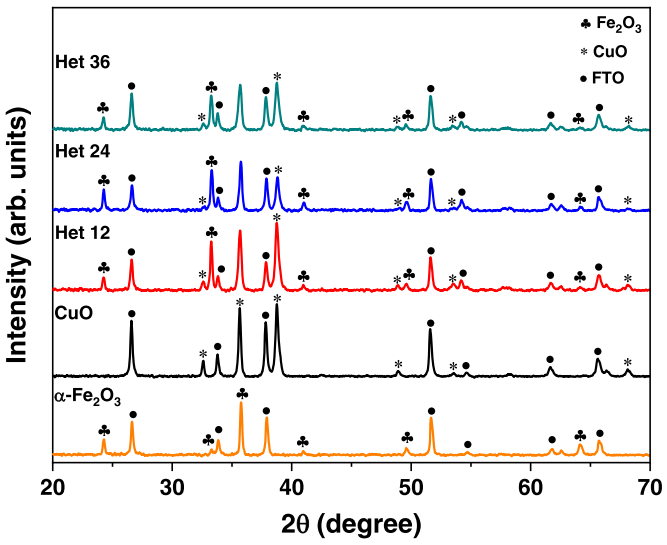

Fig. 3. XRD patterns of Het 12, Het 24, Het 36 and the pure oxides CuO and α-Fe_2O_3. The diffraction peaks corresponding to FTO substrate, CuO and α-Fe_2O_3 are marked by "●", "*" and "♣", respectively.

3.3. Atomic force microscopy

AFM was used to explore the surface topography and roughness of pristine and heterostructures samples. The 2D AFM images of α-Fe_2O_3, Het 12, Het 24 and Het 36 films deposited on FTO have been shown in Fig. 4. The bare α-Fe_2O_3 thin film deposited on FTO glass substrate (Fig. 4a) exhibited conical shape and larger particle with porous morphology [24]. The AFM images of the different heterostructures (Fig. 4b-d) displayed conical shapes similar to that obtained for pristine α-Fe_2O_3, although with larger particles compared to it. The root mean square roughness for α-Fe_2O_3, Het 12, Het 24 and Het 36 films was found to be 5.8, 10.2, 11.6 and 15.4 nm, respectively. It should be noted that in the heterostructures the α-Fe_2O_3 islands coalesced each other and grains size and shape were improved, due to the presence of the CuO film underneath [38].

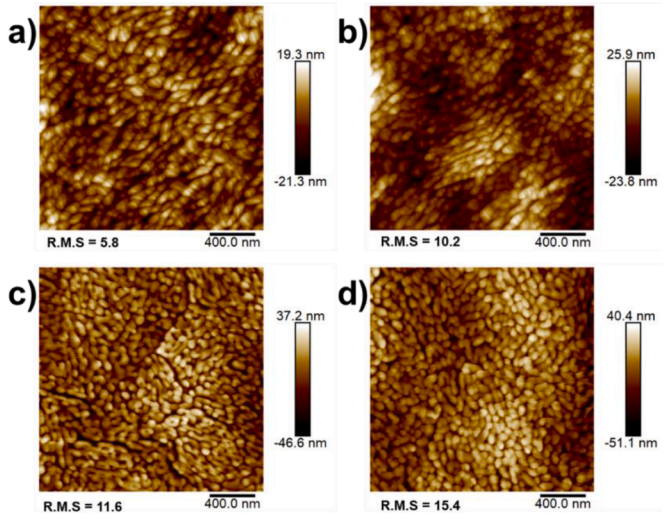

Fig. 4. The 2D AFM images of a) α-Fe_2O_3, b) Het 12, c) Het 24 and d) Het 36 thin films.

3.4. Field emission scanning electron microscopy and energy dispersive X-ray spectroscopy

Films morphology and cross-section of heterostructures were investigated by FE-SEM technique. FE-SEM top-view images of CuO films fabricated with a different number of layers 12, 24 and 36 are shown in Fig. 5a–c, respectively. As shown in Fig. 5a-c, the shape of CuO particles is quasi-spherical. Besides, the increase of the number of CuO layers produces a decrease of the mean diameter of the Het 12 compared to the size of particles that make up the Het 24 and Het 36 due to the elimination of defects and reduction of residual stress during thermal treatment [39]. The average size of the CuO films was: 86 ± 16 nm, 42 ± 5 nm, and 40 ± 11 nm for 12, 24 and 36 deposited layers, respectively. Fig. 5d-f display cross-sectional FE-SEM images of the heterostructures and thickness of bare oxides (CuO and α-Fe_2O_3) that form them. The CuO and α-Fe_2O_3 films are willing as separate materials joined only for one phase junction, demonstrated by EDS elemental maps shown in the insets in Fig. 5d, 5e and 5f. The thicknesses of α-Fe_2O_3 for the three heterostructures are almost similar to each other (~620 nm), due to the same number of α-Fe_2O_3 layers deposited on FTO glass. Furthermore, and as expected, the thicknesses of CuO films increase with increasing the number of immersions made. The values obtained were approximately 390 nm, 620 nm and 930 nm for Het 12, Het 24 and Het 36, respectively.

3.5. Optical absorption spectroscopy

The determination of the optical band gap energies for the heterostructures fabricated was estimated through Tauc's plot employing the Kubelka-Munk equation. In this model, the data of the diffuse reflectance (R) spectrum is used. Thus, the optical band gap (E_g) can be estimated from the following relation [40]:

$$F(R)h\nu = A\left(h\nu - E_g\right)^n \quad (1)$$

where $F(R)$ is the Kubelka-Munk function ($F(R) = (1-R)^2/2R$), $h\nu$ is the photon energy, E_g is the optical band gap energy and A is known as band tailing parameter which is independent of photon energy [40]. The constant (n) in Eq. (1) is the exponent depending on quantum selection rules for the particular material, for direct band transition $\eta = 0.5$ [40]. The band gap was obtained by extrapolating the linear part to zero on the ordinate axis ($h\nu$), as seen in Fig. 6. The Tauc plot and optical band gap value estimated for CuO films is given in Fig. 7a. The value calculated of approximately 1.50 eV was found to be close to the values of energy gap measured for CuO p-type thin films [41–43], where the conductivity of the films was determinate by Hall-effect demonstrating that the major carriers in CuO films were positive. In addition, most CuO are found to be p-type and this is likely related to its intrinsic defects, particularly Cu vacancies due to high volatility of Cu atoms [43].

The optical band gap values obtained are 1.51, 1.41 and 1.47 eV for Het 12, Het 24 and Het 36, respectively. The E_g for Het 12 decreased from 1.51 to 1.41 eV for Het 24 and 1.47 eV for Het 36 due to the increase in the film thickness [44]. An increase in thickness decreases defects which create localized states in the band gap and therefore decrease it [45–47]. However, the increase of the band gap from Het 24 to Het 36 is caused by the formation of a greater number of defects in the films, which produce more localized states in them. The thicker film

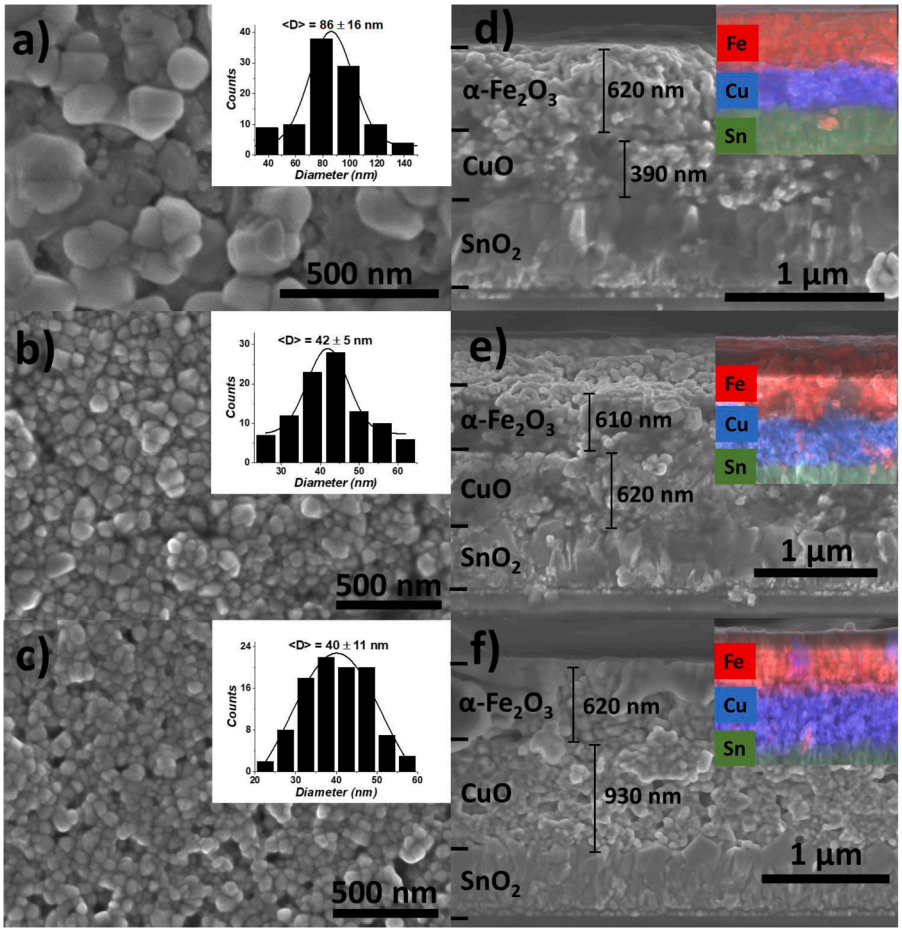

Fig. 5. FE-SEM top-view images of CuO films fabricated with a different number of layers a) 12, b) 24 and c) 36. Cross-sectional FE-SEM images of d) Het 12, e) Het 24 and f) Het 36 films. The size distributions and corresponding standard deviations are shown as insets.

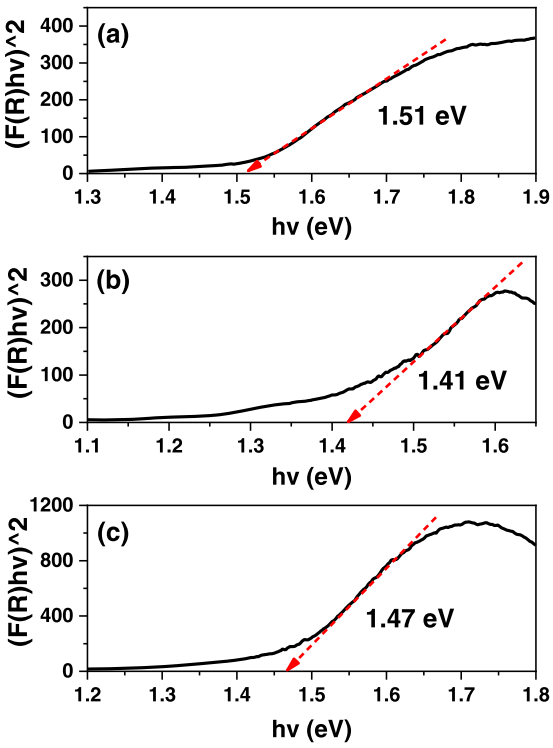

Fig. 6. Tauc plots for the estimation of optical band gaps for a) Het 12, b) Het 24 and c) Het 36 films.

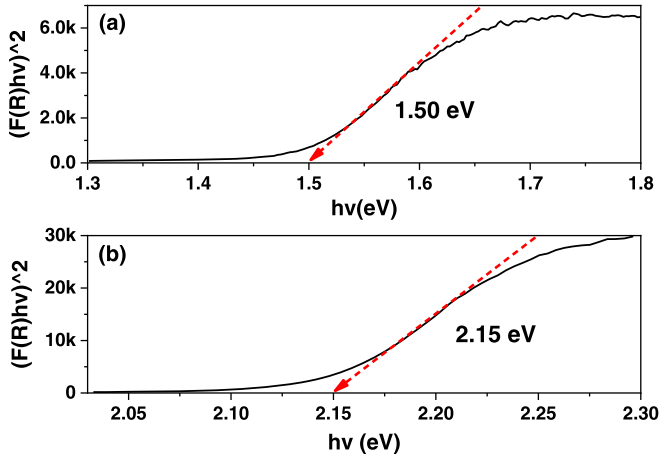

Fig. 7. Tauc plots for the estimation of optical band gaps for a) CuO and (b) α-Fe_2O_3 films.

increases the width of localized states in the optical band gap, consequently, increases the band gap [47–49]. Based on the aforementioned works [45–49] and in correlation with our results, it should be noted that a direct relationship between the film thickness and its respective band gap calculated has not yet been fully demonstrated. However, we consider the thickness as a necessary factor to determinate the optical band gap.

3.6. Photoluminescence spectroscopy study

Photoluminescence spectroscopy (PL) was carried out to investigate the separation process of electron (e^-) and hole (h^+) pairs in our heterostructures. The PL emission was mainly occurred due to the e^-–h^+ pair recombination and its intensity is directly proportional to the rate of these electron-hole pair recombination. Principally, higher PL intensity indicates faster recombination, unlike lower PL intensity, which expresses a slower or restricted recombination rate [50]. Fig. 8a shows the photoluminescence spectra with a 325 nm excitation wavelength of bare CuO, bare α-Fe_2O_3 and Het 24 film. It was found a broad emission peak around at 517 nm. The observed intensity of this peak for CuO film is many times larger than that of α-Fe_2O_3, which in turn is greater than of Het 24 indicating much slower electron-hole radiative recombination compared to pristine α-Fe_2O_3 and CuO. This reduction in the PL intensity of Het 24 can be attributed to the formation of p-n junction with matched energy levels [39]. Gao et al. [51] have explained the enhanced oxygen evolution reaction in the α-Fe_2O_3/CuO heterostructure by the electronic interaction between α-Fe_2O_3 and CuO and they have calculated the valence band energy value and Fermi level energy value (E_F) by the ultraviolet photoelectron spectra method. The E_F values calculated for CuO and α-Fe_2O_3 were -7.63 and -7.00 [51], respectively. This lower E_F of CuO than that of α-Fe_2O_3 promotes the transfer of electrons from α-Fe_2O_3 to CuO until the E_F equilibrium is reached. In this work, in the α-Fe_2O_3/CuO junction, electrons are also transferred from α-Fe_2O_3 to CuO until the E_F equilibrium is attained. At the equilibrium of the α-Fe_2O_3/CuO, the inner electric field makes the p-type CuO region negatively charged while n-type α-Fe_2O_3 positively charged. Holes move into the negative field and electrons are directed to the positive field forming a p-n junction. This junction enhances the separation of excitons as α-Fe_2O_3 transports electrons away and CuO transports the holes similar to the ZnO/CuO junction case demonstrated by previous work [52,53]. This will reduce the electron-hole recombination and reduce the PL intensity. This process may be expressed as the efficient separation of photogenerated electron-hole pairs at the p-n junction.

PL spectrums of the heterostructures in the range at 505–535 nm wavelengths are shown in Fig. 8b. The results reveal that the PL intensities of the heterostructures first decrease and then increase with increasing thickness of the CuO layers, reaching a minimum when the number of CuO layers is 24. The decrease rapidly of the PL intensity with increasing thickness is due to the strange phenomena of emissions in CuO related to electron transitions, which also occurred in another CuO thin films study [54]. Meanwhile, as the thickness of the CuO layer continues to increase, the crystallinity of Het 36 (20 layers of α-Fe_2O_3/36 layers of CuO) will be destroyed because of the number of CuO layers, leading the photoluminescence intensity increases again [55,56].

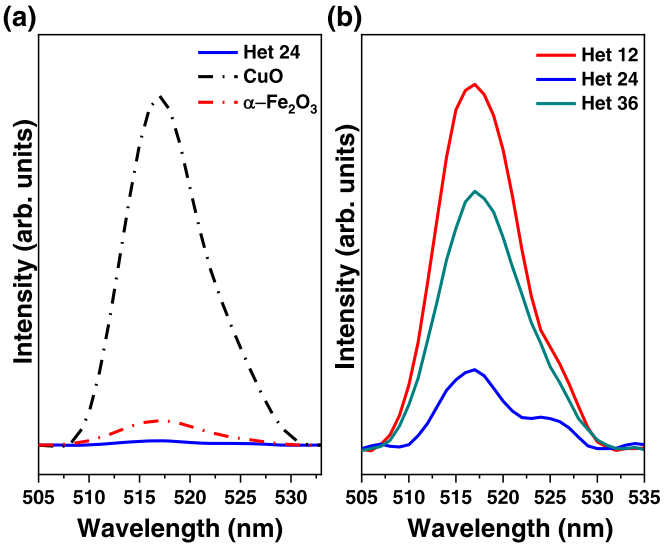

Fig. 8. a). Photoluminescence spectra for CuO, α-Fe_2O_3 and Het 24 thin films and b) PL spectra comparison between Het 12, Het 24 and Het 36 thin films.

3.7. Band alignment engineering

In order to understand the mechanism of the formation of a p–n heterostructure and the direction of flow of charge carriers in the heterostructure between n-type α-Fe_2O_3 and p-type CuO, the band edge positions, relative Fermi energy levels, and work functions of both semiconductors were estimated. These are the three important parameters used to establish the direction of flow of photogenerated charge carriers in the heterostructure. Primarily, the band edge positions of CuO and α-Fe_2O_3 were calculated using the following equations on absolute vacuum scale [57]:

$$E_{CB} = -\chi + 0.5E_g$$

$$E_{VB} = -\chi - 0.5E_g$$

Where E_{CB} and E_{VB} are the conduction and valence band edge potentials, respectively, E_g is the band gap of the semiconductor and χ is the electronegativity of the semiconductor. The calculated χ values for α-Fe_2O_3 and CuO are reported to be 5.88 eV and 5.81 eV, respectively [58]. Meanwhile, the calculated band gap values of α-Fe_2O_3 and CuO are approximately 2.15 eV and 1.50 eV, respectively (see Fig. 7). Therefore, the conduction band edge potentials for α-Fe_2O_3 and CuO were estimated to be -4.805 eV and -5.060 eV and the valence band edge potentials for α-Fe_2O_3 and CuO were calculated to be -6.955 eV and -6.560 eV, respectively.

The Fermi level of n-type semiconductor generally lies below the bottom of the conduction band (CB) by ca. 0.1 eV, whereas for p-type semiconductor the fermi level lies approximately 0.1 eV above the top of the valence band (VB) [59]. Therefore, the Fermi levels for n-type α-Fe_2O_3 and p-type CuO were calculated to be -4.905 eV and -6.460 eV, respectively. The work function (Φ) can be calculated using the equation: $\Phi = E_{VAC} - E_F$, where E_F is Fermi energy level of the semiconductor and E_{VAC}, with a value of 0 eV, is defined as the energy level of an electron with zero kinetic energy with respect to the sample surface [60]. So, the relative work functions of α-Fe_2O_3 and CuO are calculated to 4.905 eV and 6.460 eV, respectively. Finally, the work functions, CB and VB and Fermi energy levels of α-Fe_2O_3 and CuO, before contact, are represented in Fig. 9a.

When p-type CuO and n-type α-Fe_2O_3 thin films are assembled, a p–n junction is formed between them and the electrons move from n-Fe_2O_3 to p-CuO, making a negative section in the p-CuO region near the junction; holes move from p-CuO to n-Fe_2O_3, generating a positive section in the n-Fe_2O_3 region next to the junction. This process will continue until the system reaches a thermal equilibrium state; thus, an inner electric field is created at the interface, oriented in the direction from n-type α-Fe_2O_3 to p-type CuO and thus promote charge transfer in the interfacial space. Furthermore, the work function of α-Fe_2O_3 and CuO will remain the same with respect to the vacuum level after the formation of a p–n junction between them. To maintain the above condition in this process, the energy bands (the CB and VB) of CuO will not bend and are maintained the same as they were before contact; only the energy bands of α-Fe_2O_3 bend during the vacuum energy level bending. The amount of energy band bending of α-Fe_2O_3 compared to its original position in this process was determined from the subtraction between the work functions of CuO and α-Fe_2O_3 [61], obtaining the value of 1.555 eV. Consequently, the CB and VB of CuO are positioned higher than the CB and VB of α-Fe_2O_3 after the formation of a p–n junction between them, with a type-II staggered band alignment between CuO and α-Fe_2O_3, as shown in Fig. 9b.

3.8. Removal of trace arsenic (III)

The arsenic removal using the heterostructures fabricated in this work is carried out by two processes, which are photooxidation and adsorption. The possible mechanism of As(III) removal through photocatalytic oxidation and adsorption has proposed for the CuO/α-Fe_2O_3

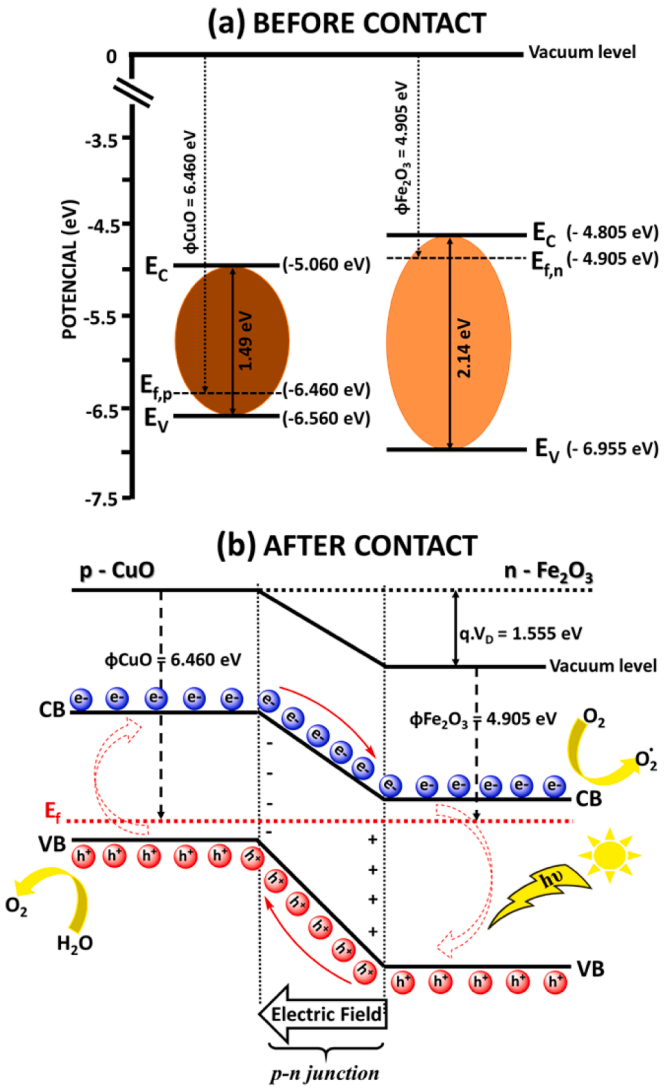

Fig. 9. (a). Diagram of the energy band positions of n-type α-Fe_2O_3 and p-type CuO before contact. (b) Formation of a p–n junction and the charge separation mechanism of the CuO/α-Fe_2O_3 p–n junction under visible light irradiation.

heterostructures, as illustrated in Fig. 10. First, when the heterostructure is irradiated with visible light, both semiconductors (CuO and α-Fe_2O_3) can be excited and produce photogenerated electron-hole pairs. Since the CB and VB positions of CuO are higher than α-Fe_2O_3 (see Fig. 10), the electron transfer occurs from the CB of light-activated CuO to the CB of light-activated α-Fe_2O_3, and conversely, the hole transfer takes place from the VB of α-Fe_2O_3 to that of CuO, which prolong the lifetime of recombination of photogenerated carriers enhancing the charge transfer [62]. Then, for the photooxidation process the As(III) molecules are mobilized by convection or diffusion towards the surface of the heterostructure. In addition, the photogenerated electrons and holes in the heterostructure could migrate to the surface where could react with the surface-absorbed water and oxygen molecules to produces the reactive oxygen species (ROS) as hydroxyl radical, superoxide anion and singlet oxygen [63], are these ROS the intermediaries to oxidize As(III) to As(V) at the solid/liquid interface [63,64], thus achieving an efficient immobilization of arsenic. In the case of adsorption, which is a simple process, the As(V) formed in the aqueous solution was transported toward to the solid/liquid interface, being adsorbed onto the surface of the heterostructure by substitution the hydroxyl group or As(III) adsorbed previously constituting the inner-sphere complexes on the surface of the heterostructure [64].

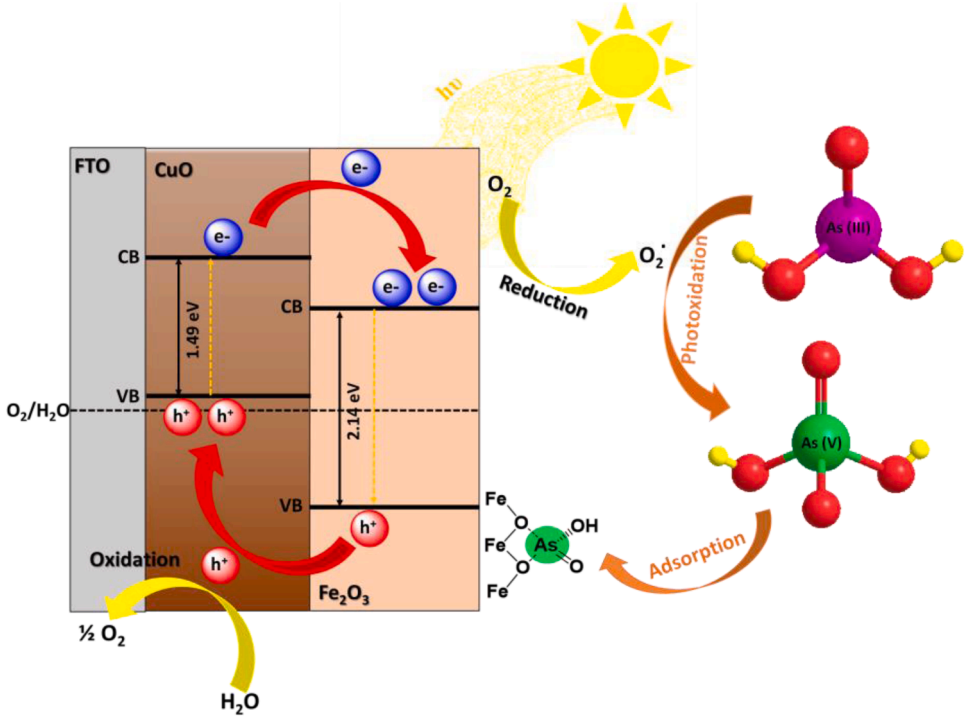

Fig. 10. The proposed arsenite removal mechanism using CuO/α-Fe_2O_3 heterostructure.

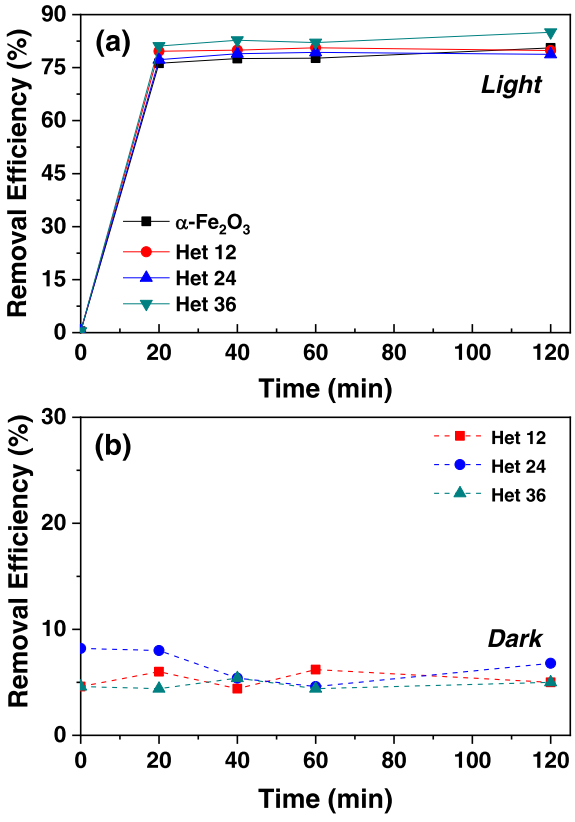

Fig. 11. Effect of contact time variation on the removal efficiency of As(III) on α-Fe_2O_3, Het 12, Het 24 and Het 36 films (T = 20 ± 1 °C, pH = 3.1, film area = 4.8 cm^2).

To investigate the efficiency of arsenite (As(III)) adsorption for bare α-Fe_2O_3 and heterostructures films, the experiments were proceeded for 2 h at 20 °C around pH 3.1. The initial concentration of As(III) was 1000 ppb and the plot of the removal efficiency of As(III) was depicted in Fig. 11a, where the As(III) removal under light irradiation occurred within the first 20 min of irradiation, after which the arsenite removal efficiency remains relatively constant for the samples obtained. The reasons for this rapid adsorption are related to the numerous active adsorption sites on the surface of nanomaterial [65], the formation of hydroxyl groups and Fe-O-As bond that makes up adsorbed surface complexes [66]. This implies a specific sorption mechanism, including complexation models according to spectroscopic investigations [66,67]. Fig. 11a also shows that the best removal arsenic efficiency under light was obtained for Het 36 followed by the efficiencies for Het 12, Het 24, and α-Fe_2O_3. The removal efficiency was found to be 80%, 79% and 85% for Het 12, Het 24 and Het 36 respectively. Moreover, it should be noted that the removal of As(III) for the heterostructures in darkness was lower compared to light experiments, with values obtained below 10% (see Fig. 11b) corroborating that the adsorption was effectively enhanced by the heterostructures photoactivity. The profile curve, in Fig. 11a, for Het 12 and Het 24 seems to be the same due to the removal efficiency percentage is almost close. Whereas, the profile for the Het 36 curve is remarkably different from the others and its removal efficiency was higher. It is thought that the reason for the highest removal efficiency of Het 36 is its high roughness compared to roughness for samples Het 12 and Het 24, as was discussed in the AFM section. The roughness can lead to increased photoactivity due to the increase in the overall catalytic surface area, which favors the increase in the number of surface defects [68]. Moreover, many researchers claim that the increase of the surface roughness may favor the adsorption of molecules on the surface films [69].

In the process to remove As(III) under light irradiation using the heterostructures and α-Fe_2O_3 films, arsenate As(V) species were originated by photooxidation of As(III). The results are shown in Fig. 12. The concentration of As(V) obtained was kept below 8ppb for all heterostructures. Furthermore, As(V) produced reached an equilibrium between oxidation/absorption of arsenic species at pH = 3.1 denoted by

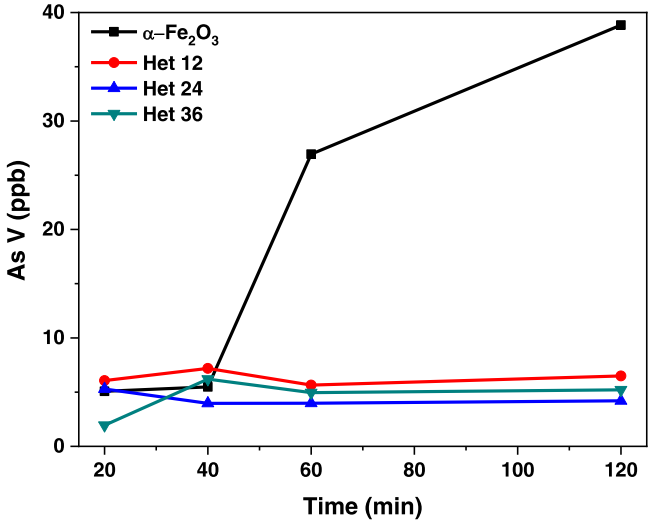

Fig. 12. Concentration of As(V) produced during the adsorption process using α-Fe_2O_3, Het 12, Het 24 and Het 36 films (T = 20 ± 1 °C, pH = 3.1, film area = 4.8 cm^2).

the stability of the curves in the last forty minutes of the experiments. At the beginning, it was possible to adsorb As(III) directly as a photooxidation to As(V) and at the same time adsorb it. Moreover, it is known that As(V) exists as an oxyanion (H_2AsO^{4-}), while As(III) arise as a neutral species (H_3AsO_3) being more difficult to immobilize than As(V)-bearing oxyanions [65]. Therefore, the process of photooxidation As(III) to As(V) is a pathway to adsorb that should be considered.

The As(V) concentration obtained for α-Fe_2O_3 film increases non-linearly with increasing the contact time to 38 ppb for 120 min. Hematite leaves at least five times more As(V) concentration values at the end of the experiments compared to heterostructures as seen in Fig. 12. Besides, previous works [70,71] reveals a similar quantitative performance for arsenic adsorption by hematite in dark or under visible light irradiation. Therefore, we believe that the photooxidation of As(III) to As(V) produces large quantities of As(V) in the system that hematite cannot remove efficiently. This clearly illustrates the lower quantum efficiency of pure α-Fe_2O_3.

4. Conclusions

In summary, a series of CuO/α-Fe_2O_3 heterostructures were prepared through the dip-coating method, varying the number of CuO layers. The FT-IR, and XRD confirmed the effective formation of the heterostructures with CuO films underneath α-Fe_2O_3 films. The thickness of the α-Fe_2O_3 in the heterostructures was found around 620 nm, while the thickness for CuO was approximately 390, 620, and 930 nm for Het 12, Het 24 and Het 36 respectively. Moreover, the band gap energy estimated by optical reflectance was 1.51, 1.41, and 1.47 eV for Het 12, Het 24, and Het 36 respectively. PL measurements confirmed the slower electron-hole pairs recombination for the heterostructures compared to the pure oxides. The heterostructures present fast and efficient arsenic removal performances, due to its rough structure. The arsenic (III) removal was attributed to the direct absorption on thin films and/or photooxidation of As(III) to As (V). The highest removal efficiency of As (III) in aqueous systems was obtained for the heterostructure Het 36.

Author contribution statement

Elizabeth C. Pastrana: Conceptualization, Methodology, Validation, Writing original draft, Formal analysis, Investigation, Data curation, Writing-reviewers and Editing. **Steveen J. Loarte**: Investigation, Formal analysis, Data curation. **Carlos D. Gonzales-Lorenz**: Visualization, Formal analysis, Resources. **Roxana Y. P. Alta**: Visualization, Supervision, Resources. **Hugo A. Alarcón**: Supervision, Resources, Project administration, Funding acquisition.

Declaration of Competing Interest

The authors declare that they have no known competing financial interests or personal relationships that could have appeared to influence the work reported in this paper.

Acknowledgments

The work described in this paper was financially supported by the National Fund for the Scientific and Technological Development (FONDECYT), Grant No. 237–2015-FONDECYT. The authors thank Dr. Breno Pannia Espósito and the LABQAM of the Chemistry Institute of USP for the analysis of the samples. In addition, authors thank Dr. Pierre Ramos Apestegui for his excellent technical assistance with scanning electron microscopy observation.

References

[1] S. Fendorf, H.A. Michael, A. van Geen, Spatial and temporal variations of groundwater arsenic in South and Southeast Asia, Science 328 (2010) 1123–1127, https://doi.org/10.1126/science.1172974.
[2] K.K. Sodhi, M. Kumar, P.K. Agrawal, D.K. Singh, Perspectives on arsenic toxicity, carcinogenicity and its systemic remediation strategies, Environ. Technol. Innov. 16 (2019), 100462, https://doi.org/10.1016/j.eti.2019.100462.
[3] B.Z. Can, R. Boncukcuoglu, A.E. Yilmaz, B.A. Fil, Effect of some operational parameters on the arsenic removal by electrocoagulation using iron electrodes, J. Environ. Health Sci. Engineer. 12 (2014) 95, https://doi.org/10.1186/2052-336X-12-95.
[4] S.M. Prabhu, S. Kancharla, C.M. Park, K. Sasaki, Synthesis of modulator-driven highly stable zirconium-fumarate frameworks and mechanistic investigations of their arsenite and arsenate adsorption from aqueous solutions, CrystEngComm 21 (2019) 2320–2332, https://doi.org/10.1039/C8CE01424H.
[5] M. Shafiquzzaman, M.S. Azam, J. Nakajima, Q.H. Bari, Investigation of arsenic removal performance by a simple iron removal ceramic filter in rural households of Bangladesh, Desalination 265 (2011) 60–66, https://doi.org/10.1016/j.desal.2010.07.031.
[6] B.V. Tangahu, S.R. Sheikh Abdullah, H. Basri, M. Idris, N. Anuar, M. Mukhlisin, A review on heavy metals (As, Pb, and Hg) uptake by plants through phytoremediation, Int. J. Chem. Eng. (2011) (2011) 1–32, https://doi.org/10.1155/2011/939161.
[7] M. Bissen, M.-M. Vieillard-Baron, A.J. Schindelin, F.H. Frimmel, TiO_2-catalyzed photooxidation of arsenite to arsenate in aqueous samples, Chemosphere 44 (2001) 751–757, https://doi.org/10.1016/S0045-6535(00)00489-6.
[8] R. Kumar, M. Patel, P. Singh, J. Bundschuh, C.U. Pittman Jr, L. Trakal, D. Mohan, Emerging technologies for arsenic removal from drinking water in rural and peri-urban areas: Methods, experience from, and options for Latin America, Sci. Total Environ. 694 (2019), 133427, https://doi.org/10.1016/j.scitotenv.2019.07.233.
[9] D. Mohanty, Conventional as well as emerging arsenic removal technologies—a critical review, Water Air Soil Pollut. 228 (2017) 381, https://doi.org/10.1007/s11270-017-3549-4.
[10] N.R. Nicomel, K. Leus, K. Folens, P. Van Der Voort, G. Du Laing, Technologies for arsenic removal from water: current status and future perspectives, Int. J. Environ. Res. Public Health. 13 (2016) 62, https://doi.org/10.3390/ijerph13010062.
[11] M.R. Yazdani, T. Tuutijärvi, A. Bhatnagar, R. Vahala, Adsorptive removal of arsenic (V) from aqueous phase by feldspars: kinetics, mechanism, and thermodynamic aspects of adsorption, J. Mol. Liq. 214 (2016) 149–156, https://doi.org/10.1016/j.molliq.2015.12.002.
[12] Y. Yin, T. Zhou, H. Luo, J. Geng, W. Yu, Z. Jiang, Adsorption of arsenic by activated charcoal coated zirconium-manganese nanocomposite: performance and mechanism, Colloids Surf. A Physicochem. Eng. Asp 575 (2019) 318–328, https://doi.org/10.1016/j.colsurfa.2019.04.093.
[13] T. Sun, Z. Zhao, Z. Liang, J. Liu, W. Shi, F. Cui, Efficient As, removal by magnetic CuO-Fe_3O_4 nanoparticles through photo-oxidation and adsorption under light irradiation, J. Colloid Interface Sci 495 (2017) 168–177, https://doi.org/10.1016/j.jcis.2017.01.104.
[14] H. Eslami, M.H. Ehrampoush, A. Esmaeili, A.A. Ebrahimi, M.H. Salmani, M. T. Ghaneian, H. Falahzadeh, Efficient photocatalytic oxidation of arsenite from contaminated water by Fe_2O_3-Mn_2O_3 nanocomposite under UVA radiation and process optimization with experimental design, Chemosphere 207 (2018) 303–312, https://doi.org/10.1016/j.chemosphere.2018.05.106.
[15] J.S. Zhang, R.S. Stanforth, S.O. Pehkonen, Effect of replacing a hydroxyl group with a methyl group on arsenic (V) species adsorption on goethite (α-FeOOH), J. Colloid Interface Sci 306 (2007) 16–21, https://doi.org/10.1016/j.jcis.2006.10.004.

[16] D. Dickson, G. Liu, Y. Cai, Adsorption kinetics and isotherms of arsenite and arsenate on hematite nanoparticles and aggregates, J. Environ. Manage. 186 (2017) 261–267, https://doi.org/10.1016/j.jenvman.2016.07.068.

[17] A.Y. Oral, E. Menşur, M.H. Aslan, E. Başaran, The preparation of copper(II) oxide thin films and the study of their microstructures and optical properties, Mater. Chem. Phys 83 (2004) 140–144, https://doi.org/10.1016/j.matchemphys.2003.09.015.

[18] Y.-F. Lim, C.S. Chua, C.J.J. Lee, D. Chi, Sol–gel deposited Cu_2O and CuO thin films for photocatalytic water splitting, Phys. Chem. Chem. Phys 16 (2014) 25928–25934, https://doi.org/10.1039/C4CP03241A.

[19] Y.H. Navale, S.T. Navale, F.J. Stadler, N.S. Ramgir, V.B. Patil, Enhanced NO_2 sensing aptness of ZnO nanowire/CuO nanoparticle heterostructure-based gas sensors, Ceram. Int. 45 (2019) 1513–1522, https://doi.org/10.1016/j.ceramint.2018.10.022.

[20] J. Deng, L. Wang, Z. Lou, T. Zhang, Design of CuO–TiO_2 heterostructure nanofibers and their sensing performance, J. Mater. Chem. A 2 (2014) 9030–9034, https://doi.org/10.1039/C4TA00160E.

[21] G. Zhang, Z. Ren, X. Zhang, J. Chen, Nanostructured iron(III)-copper(II) binary oxide: a novel adsorbent for enhanced arsenic removal from aqueous solutions, Water Res. 47 (2013) 4022–4031, https://doi.org/10.1016/j.watres.2012.11.059.

[22] S. Krehula, M. Ristić, Z. Petrović, L.K. Krehula, I. Mitar, S. Musić, Effects of Cu doping on the microstructural, thermal, optical and photocatalytic properties of α-FeOOH and α-Fe_2O_3 1D nanoparticles, J. Alloys Compd. 802 (2019) 290–300, https://doi.org/10.1016/j.jallcom.2019.06.133.

[23] E.L. Tsege, T.Sh. Atabaev, Md.A. Hossain, D. Lee, H.-K. Kim, Y.-H. Hwang, Cu-doped flower-like hematite nanostructures for efficient water splitting applications, J. Phys. Chem. Solids 98 (2016) 283–289, https://doi.org/10.1016/j.jpcs.2016.07.014.

[24] E.C. Pastrana, V. Zamora, D. Wang, H. Alarcón, Fabrication and characterization of α-Fe_2O_3/CuO heterostructure thin films via dip-coating technique for improved photoelectrochemical performance, Adv. Nat. Sci: Nanosci. Nanotechnol. 10 (2019), 035012, https://doi.org/10.1088/2043-6254/ab3d2f.

[25] Y. Gao, N. Zhang, C. Wang, F. Zhao, Y. Yu, Construction of Fe_2O_3@CuO heterojunction nanotubes for enhanced oxygen evolution reaction, ACS Appl. Energy Mater. 3 (2019) 666–674, https://doi.org/10.1021/acsaem.9b01866.

[26] E. Alp, H. Eşgin, M.K. Kazmanlı, A. Genç, Synergetic activity enhancement in 2D CuO-Fe_2O_3 nanocomposites for the photodegradation of rhodamine B, Ceram. Int 45 (2019) 9174–9178, https://doi.org/10.1016/j.ceramint.2019.01.258.

[27] J.T. Mayo, C. Yavuz, S. Yean, L. Cong, H. Shiple, W. Yu, J. Falkner, A. Kan, M. Tomson, V.L. Colvin, The effect of nanocrystalline magnetite size on arsenic removal, Sci. Technol. Adv. Mater. 8 (2007) 71, https://doi.org/10.1016/j.stam.2006.10.005.

[28] S.S. Shariffudin, S.S. Khalid, N.M. Sahat, M.S.P. Sarah, H. Hashim, Preparation and characterization of nanostructured CuO thin films using Sol-Gel dip coating, IOP Conf. Ser. Mater. Sci. Eng. 99 (2015), 012007, https://doi.org/10.1088/1757-899X/99/1/012007.

[29] A. Karakuscu, M. Ozenbas, Characterization of iron oxide thin films prepared by Sol–Gel processing, J. Nanosci. Nanotechnol 8 (2008) 901–906, https://doi.org/10.1166/jnn.2008.D027.

[30] R. Dobrucka, Antioxidant and catalytic activity of biosynthesized CuO nanoparticles using extract of *Galeopsidis herba*, J. Inorg. Organomet. Polym. Mater. 28 (2018) 812–819, https://doi.org/10.1007/s10904-017-0750-2.

[31] V. Gopinath, S. Priyadarshini, A.R. Al-Maleki, M. Alagiri, R. Yahya, S. Saravanan, J. Vadivelu, *In vitro* toxicity, apoptosis and antimicrobial effects of phyto-mediated copper oxide nanoparticles, RSC Adv. 6 (2016) 110986–110995, https://doi.org/10.1039/C6RA13871C.

[32] A.A. Jacob, L. Balakrishnan, S.R. Meher, R. Sivacoumar, K. Shambavi, Z.C. Alex, Ammonia, acetone and ethanol gas sensing characteristics of CuO thin films grown by sputtering, IOP Conf. Ser. Mater. Sci. Eng. 360 (2018), 012062, https://doi.org/10.1088/1757-899X/360/1/012062.

[33] F. Wang, X.F. Qin, Y.F. Meng, Z.L. Guo, L.X. Yang, Y.F. Ming, Hydrothermal synthesis and characterization of α-Fe_2O_3 nanoparticles, Mater. Sci. Semicond. Process. 16 (2013) 802–806, https://doi.org/10.1016/j.mssp.2012.12.029.

[34] R.N. Mariammal, K. Ramachandran, Study on gas sensing mechanism in p-CuO/n-ZnO heterojunction sensor, Mater. Res. Bull. 100 (2018) 420–428, https://doi.org/10.1016/j.materresbull.2017.12.046.

[35] D.K. Bandgar, S.T. Navale, Y.H. Navale, S.M. Ingole, F.J. Stadler, N. Ramgir, D. K. Aswal, S.K. Gupta, R.S. Mane, V.B. Patil, Flexible camphor sulfonic acid-doped PAni/α-Fe_2O_3 nanocomposite films and their room temperature ammonia sensing activity, Mater. Chem. Phys. 189 (2017) 191–197, https://doi.org/10.1016/j.matchemphys.2016.12.050.

[36] S. Takai, E. Sawada, J. Harada, S. Park, M. Oda, S. Esaki, M. Nishijima, T. Yoshie, T. Yabutsuka, T. Yao, Synthesis and anode properties of corundum-type structured $(Fe_2O_3)_{1-x}(Al_2O_3)_x$ solid solutions in the whole compositional range, Solid State Ion 313 (2017) 1–6, https://doi.org/10.1016/j.ssi.2017.10.026.

[37] P. Vinothkumar, C. Manoharan, B. Shanmugapriya, M. Bououdina, Effect of reaction time on structural, morphological, optical and photocatalytic properties of copper oxide (CuO) nanostructures, J. Mater. Sci. Mater. Electron. 30 (2019) 6249–6262, https://doi.org/10.1007/s10854-019-00928-7.

[38] H. Lahmar, F. Setifi, A. Azizi, G. Schmerber, A. Dinia, On the electrochemical synthesis and characterization of p-Cu_2O/n-ZnO heterojunction, J. Alloys Compd. 718 (2017) 36–45, https://doi.org/10.1016/j.jallcom.2017.05.054.

[39] S.K. Lakhera, A. Watts, H.Y. Hafeez, B. Neppolian, Interparticle double charge transfer mechanism of heterojunction α-Fe_2O_3/Cu_2O mixed oxide catalysts and its visible light photocatalytic activity, Catal. Today 300 (2018) 58–70, https://doi.org/10.1016/j.cattod.2017.03.020.

[40] R.V. Vijayalakshmi, G. Saravanan, P.P. Kumar, K. Ravichandran, Systematic analysis of CuO and Co doped CuO nanoparticles and the impact of dopant on magnetic and optical properties, AIP Conf. Proc. 1953 (2018), 030160, https://doi.org/10.1063/1.5032495.

[41] M.G. Faraj, A.K. Kaka, H.D. Omar, Electrical and structural properties of copper oxide (CuO) thin films on plastic substrate deposited by spray pyrolysis technique, ARO- Sci. J. Koya Univ. 7 (2019) 14–18, https://doi.org/10.14500/aro.10558.

[42] L. De los Santos Valladares, D. Hurtado Salinas, A. Bustamante Dominguez, D. Acosta Najarro, S.I. Khondaker, T. Mitrelias, C.H.W. Barnes, J. Albino Aguiar, Y. Majima, Crystallization and electrical resistivity of Cu_2O and CuO obtained by thermal oxidation of Cu thin films on SiO_2/Si substrates, Thin Solid Films 520 (2012) 6368–6374, https://doi.org/10.1016/j.tsf.2012.06.043.

[43] X. Hu, F. Gao, Y. Xiang, H. Wu, X. Zheng, J. Jiang, J. Li, H. Yang, S. Liu, Influence of oxygen pressure on the structural and electrical properties of CuO thin films prepared by pulsed laser deposition, Mater. Lett. 176 (2016) 282–284, https://doi.org/10.1016/j.matlet.2016.04.055.

[44] E.S.M. Goh, T.P. Chen, C.Q. Sun, Y.C. Liu, Thickness effect on the band gap and optical properties of germanium thin films, AIP Conf. Proc. 107 (2010), 024305, https://doi.org/10.1063/1.3291103.

[45] A.Z. Mahmoud, A.A.A. Darwish, S.I. Qashou, Film thickness effects on nanorods organic films of azo quinoline derivatives for optical applications, Prog. Nat. Sci. 29 (2019) 402–409, https://doi.org/10.1016/j.pnsc.2019.04.009.

[46] S. Sönmezoğlu, A. Arslan, T. Serin, N. Serin, The effects of film thickness on the optical properties of TiO_2–SnO_2 compound thin films, Phys. Scr. 84 (2011), 065602, https://doi.org/10.1088/0031-8949/84/06/065602.

[47] M.G. Varnamkhasti, H.R. Fallah, M. Mostajaboddavati, A. Hassanzadeh, Influence of Ag thickness on electrical, optical and structural properties of nanocrystalline MoO_3/Ag/ITO multilayer for optoelectronic applications, Vacuum 86 (2012) 1318–1322, https://doi.org/10.1016/j.vacuum.2011.12.002.

[48] S.R. Ovshinsky, D. Adler, Local structure, bonding, and electronic properties of covalent amorphous semiconductors, Contemp. Phys 19 (1978) 109–126, https://doi.org/10.1080/00107517808210876.

[49] M. Rashad, A.A.A. Darwish, A.A. Attia, Impact of film thickness on optical and electrical transport properties of noncrystalline $GeSe_{1.4}Sn_{0.6}$ films, J. Non-Cryst. Solids 470 (2017) 1–7, https://doi.org/10.1016/j.jnoncrysol.2017.04.015.

[50] P.S. Kumar, M. Selvakumar, S.G. Babu, S. Induja, S. Karuthapandian, CuO/ZnO nanorods, An affordable efficient p-n heterojunction and morphology dependent photocatalytic activity against organic contaminants, J. Alloys Compd. 701 (2017) 562–573, https://doi.org/10.1016/j.jallcom.2017.01.126.

[51] Y. Gao, N. Zhang, C. Wang, F. Zhao, Y. Yu, Construction of Fe_2O_3@CuO heterojunction nanotubes for enhanced oxygen evolution reaction, ACS Appl. Energy Mater. 3 (2020) 666–674, https://doi.org/10.1021/acsaem.9b01866.

[52] J. Varghese, R. Vinodkumar, Effect of CuO on the photoluminescence quenching and photocatalytic activity of ZnO multilayered thin films prepared by sol-gel spin coating technique, Mater. Res. Express 6 (2019), 106405, https://doi.org/10.1088/2053-1591/ab3596.

[53] B.B. Sapkota, S.R. Mishra, A simple ball milling method for the preparation of *p*-CuO/*n*-ZnO nanocomposite photocatalysts with high photocatalytic activity, J. Nanosci. Nanotechnol. 13 (2013) 6588–6596, https://doi.org/10.1166/jnn.2013.7544.

[54] L. Xu, G. Zheng, S. Pei, J. Wang, Investigation of optical bandgap variation and photoluminescence behavior in nanocrystalline CuO thin films, Optik 158 (2018) 382–390, https://doi.org/10.1016/j.ijleo.2017.12.138.

[55] K. Ou, S. Wang, G. Wan, M. Huang, Y. Zhang, L. Bai, L. Yi, A study of structural, morphological and optical properties of nanostructured ZnSe/ZnS multilayer thin films, J. Alloys Compd. 726 (2017) 707–711, https://doi.org/10.1016/j.jallcom.2017.08.036.

[56] K. Ou, S. Wang, M. Huang, Y. Zhang, Y. Wang, X. Duan, L. Yi, Influence of thickness and annealing on photoluminescence of nanostructured ZnSe/ZnS multilayer thin films prepared by electron beam evaporation, J. Lumin. 199 (2018) 34–38, https://doi.org/10.1016/j.jlumin.2018.03.014.

[57] M. Alizadeh, G.B. Tong, K.W. Qadir, M.S. Mehmood, R. Rasuli, Cu_2O/InGaN heterojunction thin films with enhanced photoelectrochemical activity for solar water splitting, Renew. Energy 156 (2020) 602–609, https://doi.org/10.1016/j.renene.2020.04.107.

[58] Y. Xu, M.A.A. Schoonen, The absolute energy positions of conduction and valence bands of selected semiconducting minerals, Am. Minera 85 (2000) 543–556, https://doi.org/10.2138/am-2000-0416.

[59] Y.L. Li, Y. Liu, Y.J. Hao, X.J. Wang, R.H. Liu, F.T. Li, Fabrication of core-shell BiVO4@Fe_2O_3 heterojunctions for realizing photocatalytic hydrogen evolution via conduction band elevation, Mater. Des. 187 (2020), 108379, https://doi.org/10.1016/j.matdes.2019.108379.

[60] A. Kahn, Fermi level, work function and vacuum level, Mater. Horiz. 3 (2016) 7–10, https://doi.org/10.1039/C5MH00160A.

[61] K.H. Reddy, K. Parida, P.K. Satapathy, CuO/PbTiO: A new-fangled p–n junction designed for the efficient absorption of visible light with augmented interfacial charge transfer, photoelectrochemical and photocatalytic activities, J. Mater. Chem. A 5 (2017) 20359–20373, https://doi.org/10.1039/C7TA05206E.

[62] P.G. Ramos, C. Luyo, L.A. Sánchez, E.D. Gomez, J.M. Rodriguez, The spinning voltage influence on the growth of ZnO-rGO nanorods for photocatalytic degradation of methyl orange dye, Catalysts 10 (2020) 660, https://doi.org/10.3390/catal10060660.

[63] J. Xu, J. Li, F. Wu, Y. Zhang, Rapid photooxidation of As(III) through surface complexation with nascent colloidal ferric hydroxide, Environ. Sci. Technol. 48 (2014) 272–278, https://doi.org/10.1021/es403667b.

[64] T. Zhang, J. Wang, W. Zhang, C. Yang, L. Zhang, W. Zhu, J. Sun, G. Li, T. Li, J. Wang, Amorphous Fe/Mn bimetal–organic frameworks, outer and inner structural designs for efficient arsenic(iii) removal, J. Mater. Chem. A 7 (2019) 2845–2854, https://doi.org/10.1039/C8TA10394A.

[65] X.-Y. Yu, T. Luo, Y. Jia, Y.-X. Zhang, J.-H. Liu, X.-J. Huang, Porous hierarchically micro-/nanostructured MgO: morphology control and their excellent performance in As(III) and As(V) removal, J. Phys. Chem. C 115 (2011) 22242–22250, https://doi.org/10.1021/jp207572y.

[66] Z. Liu, J. Chen, Y. Wu, Y. Li, J. Zhao, P. Na, Synthesis of magnetic orderly mesoporous α-Fe_2O_3 nanocluster derived from MIL-100(Fe) for rapid and efficient arsenic(III,V) removal, J. Hazard. Mater. 343 (2018) 304–314, https://doi.org/10.1016/j.jhazmat.2017.09.047.

[67] Y. Mamindy-Pajany, C. Hurel, N. Marmier, M. Roméo, Arsenic adsorption onto hematite and goethite, C. R. Chim. 12 (2009) 876–881, https://doi.org/10.1016/j.crci.2008.10.012.

[68] C.S. Yaw, A.K. Soh, M.N. Chong, Effect of deposition time on the photoelectrochemical properties of cupric oxide thin films synthesized via electrodeposition method, Matec Web Conf. 60 (2016) 01001, https://doi.org/10.1051/matecconf/20166001001.

[69] J.N. Cabrera, M.M. Ruiz, M. Fascio, N. D'Accorso, R. Mincheva, P. Dubois, L. Lizarraga, R.M. Negri, Increased surface roughness in polydimethylsiloxane films by physical and chemical methods, Polymers 9 (2017) 331, https://doi.org/10.3390/polym9080331.

[70] S.L. Shumlas, S. Singireddy, A.C. Thenuwara, N.H. Attanayake, R.J. Reeder, D. R. Strongin, Oxidation of arsenite to arsenate on birnessite in the presence of light, Geochem. Trans. 17 (2016) 5, https://doi.org/10.1186/s12932-016-0037-5.

[71] S. Sun, C. Ji, L. Wu, S. Chi, R. Qu, Y. Li, Y. Lu, C. Sun, Z. Xue, Facile one-pot construction of α-Fe_2O_3/g-C_3N_4 heterojunction for arsenic removal by synchronous visible light catalysis oxidation and adsorption, Mater. Chem. Phys 194 (2017) 1–8, https://doi.org/10.1016/j.matchemphys.2017.03.023.